energies

MDPI

Article

Wing Deformation of an Airborne Wind Energy System in Crosswind Flight Using High-Fidelity Fluid–Structure Interaction

Niels Pynaert [1,2], Thomas Haas [1,2], Jolan Wauters [1,2], Guillaume Crevecoeur [1,2] and Joris Degroote [1,2]*

[1] Department of Electromechanical, Systems and Metal Engineering, Faculty of Engineering and Architecture, Ghent University, Sint-Pietersnieuwstraat 41, 9000 Gent, Belgium
[2] Core Lab MIRO, Flanders Make, 9000 Ghent, Belgium
* Correspondence: joris.degroote@ugent.be

Abstract: Airborne wind energy (AWE) is an emerging technology for the conversion of wind energy into electricity. There are many types of AWE systems, and one of them flies crosswind patterns with a tethered aircraft connected to a generator. The objective is to gain a proper understanding of the unsteady interaction of air and this flexible and dynamic system during operation, which is key to developing viable, large AWE systems. In this work, the effect of wing deformation on an AWE system performing a crosswind flight maneuver was assessed using high-fidelity time-varying fluid–structure interaction simulations. This was performed using a partitioned and explicit approach. A computational structural mechanics (CSM) model of the wing structure was coupled with a computational fluid dynamics (CFD) model of the wing aerodynamics. The Chimera/overset technique combined with an arbitrary Lagrangian–Eulerian (ALE) formulation for mesh deformation has been proven to be a robust approach to simulating the motion and deformation of an airborne wind energy system in CFD simulations. The main finding is that wing deformation in crosswind flights increases the symmetry of the spanwise loading. This property could be used in future designs to increase the efficiency of airborne wind energy systems.

Keywords: airborne wind energy; fluid–structure interaction; computational fluid dynamics; Chimera

Citation: Pynaert, N.; Haas, T.; Wauters, J.; Crevecoeur, G.; Degroote, J. Wing Deformation of an Airborne Wind Energy System in Crosswind Flight Using High-Fidelity Fluid–Structure Interaction. *Energies* **2023**, *16*, 602. https://doi.org/10.3390/en16020602

Academic Editor: Hussein A. Mohammed

Received: 8 November 2022
Revised: 21 December 2022
Accepted: 30 December 2022
Published: 4 January 2023

1. Introduction

Airborne wind energy (AWE) aims at converting wind energy into electricity using airborne devices. Currently, different types of AWE systems exist, and one of them flies crosswind patterns with an aircraft connected to a generator with a tether. The airborne device can be a soft kite or a fixed wing and the energy conversion can take place on board or on the ground [1]. This research focuses on fixed-wing aircraft systems with on-ground conversion. The flight tests documented in [2] show that it is vital to understand the interaction of unsteady aerodynamics and this dynamic system when developing large AWE systems. This interaction can be expected to increase as the size of the systems increases. Unsteady aerodynamic phenomena that can arise when operating an AWE system are fluid–structure interactions (e.g., flutter), unsteady rigid body motion of the aircraft (e.g., varying velocity), wake interactions, and fast changes in atmospheric conditions such as turbulence and gusts. To predict these phenomena and obtain insight into the design and operation of advanced and efficient AWE systems, high-fidelity tools are needed. In this work, a framework is presented that allows one to simulate these unsteady phenomena using high-fidelity tools, with a particular focus on fluid–structure interaction (FSI) in crosswind flight. The long-term goal is to realize high-fidelity simulations that can be a virtual wind tunnel for the development of increasingly large AWE systems.

In Table 1, selected literature works on AWE simulation and modeling are summarized according to the field of study and level of fidelity. For AWE systems, different fields, such as aerodynamics, structural engineering and control, are highly connected, and in order

to make accurate models, these fields should be considered together. Models of different levels of fidelity have been developed. The level of fidelity depends on the purpose of the model. In an earlier design phase, low-fidelity models are typically used to quickly iterate among different design options. In a later design stage, high-fidelity models are needed to evaluate a specific design in the most accurate way. Because full-scale testing is very expensive for airborne wind energy systems, it is expected that high-fidelity models will be crucial in the final design stage of large airborne wind energy systems.

Table 1. Matrix of state-of-the-art AWE models (S, steady; U, unsteady).

Field of Study		Low Fidelity	Mid-Fidelity	High Fidelity
AWESs	Aero	S: [3,4]	S: [5–7], U: [8]	S: [9,10], U: [11,12]
	Structure	[3]	[6]	[5,7,9]
	FSI	[3,5,7]	[6]	[9,13]
Atmosphere		[12,14,15]		[4] (LES), [12] (RANS)
Dynamics		[8]	[4,16]	[5,17]

In Table 1, we review several levels of fidelity for different fields. In aerodynamics, low-fidelity models are based on the lifting-line techniques or look-up tables. Panel methods are considered as mid-fidelity models and CFD as high-fidelity models. Regarding the structure, an Euler–Bernoulli beam model is considered to have low fidelity, the Timonshenko beam model to have mid-fidelity and finite element methods to have high fidelity. In FSI models, the fidelity depends on the fidelity of the aerodynamic and structural models. In the atmospheric model, a low-fidelity model is one described using analytical formulations and a high-fidelity model one described using CFD. Regarding aircraft motion, low-fidelity dynamic models are kinematic or quasi-steady formulations. Mid-fidelity models consider 3DOF (translational dynamics) and high-fidelity models 6DOF (translational and rotational dynamics). The models provided in Table 1 combine aircraft motion with either a detailed atmosphere or an aircraft model. A more elaborate review can be found in [18].

Current research on fluid–structure interaction for AWE is rather limited, and steady wind profile and horizontal flight are often assumed in state-of-the-art techniques. To the best of the authors' knowledge, the work by Fasel et al. [5] is the only work on FSI in AWE systems that combines flight dynamics and control. In particular, the focus of the study is on the aeroelastic optimization of a morphing AWE wing. The analysis method considers a two-way weakly coupled 3D static aeroelastic analysis model using a mid-fidelity aerodynamic method and a 3D finite element structural model. A validated FSI model of a large airborne wind turbine was developed by Wijnja et al. [3], and the aeroelastic effect of two bridle lines was analyzed in detail. The developed model is an extension of the aero-servo-elastic code ASWING. ASWING uses a lifting-line 3D representation with an unsteady flow model. In that analysis, however, only a horizontal steady flight is considered without relevant flight dynamics. An aero-structural model for a composite swept wing (semi-rigid) was developed by Candade et al. [6], with the goal of design space exploration. A structural model using Timoshenko beam theory is coupled with a non-linear vortex lattice method (VLM). Folkersma et al. [9] developed a high-fidelity FSI model of a ram-air wing by coupling a CFD solver with a finite element (FE) solver assuming steady-state flight. Hall [13] developed a high-fidelity FSI simulation to study gust load alleviation under a horizontal flight condition. No high-fidelity FSI models have been developed by combining crosswind flight dynamics. In the related field of horizontal-axis wind turbines, unsteady high-fidelity FSI simulation techniques were developed by Santo et al. [19] and Grinderslev et al. [20] by taking into account the rotational motion of wind turbines.

The aerodynamics of AWE systems were studied by Vimalakthan et al. [11] and Viré et al. [10] using CFD, but they also considered steady aerodynamics, without taking into account the crosswind motion of AWE systems or other unsteady effects. Castro-Fernández

et al. [8] took the crosswind motion into account by coupling the prescribed motion of the kite with an unsteady panel method.

Similar to wind turbines, AWE systems have a wake. Haas et al. [4] found that the wakes of utility-scale AWE systems are non-negligible. Furthermore, on-ground conversion systems or pumping-mode systems can interact with their own wakes during the reel-out phase. In [4], the dynamic motion of an AWE system was considered with the low-fidelity modeling of AWES aerodynamics using actuator methods and steady airfoil coefficients in a large-eddy simulation (LES) of wind. Kheiri et al. [12] analyzes the wake flow of an AWE system using unsteady Reynolds-average Navier–Stokes (RANS) for both AWE system aerodynamics and wind simulation. Efforts were made by Kaufman-Martin et al. [14] and Gaunaa et al. [15] to develop low-cost models for AWE wake and induction.

Table 1 indicates a gap in high-fidelity AWE models that consider aircraft, atmosphere and dynamics together. This research aimed to fill this gap by developing high-fidelity models using coupled CFD (aerodynamics and atmosphere) and finite element method (FEM), and crosswind flight maneuvers. In this work, a framework that couples the structural model of the reference aircraft presented in [7] with a CFD model was developed. In the CFD model, the aerodynamics close to the AWE wing are considered together with a logarithmic wind field. The fluid and structural models are coupled using a partitioned and explicit approach. The mesh motion in the fluid domain is implemented using a diffusion equation. Within the CFD model, the Chimera/overset technique is used to couple the wing component mesh with the background mesh by interpolating at the overset boundary. This technique allows one to take into account large rigid-body motion while maintaining constant mesh quality. The Chimera/overset technique was proven successful for horizontal-axis wind turbines in [19], but requires new developments to be applicable to complex AWE maneuvers.

The outline of this paper is as follows: The methodology is explained in Section 2. Results are presented and discussed in Section 3. Finally, Section 4 provides the conclusions and the outlook for future work.

2. Methodology

The outline of the methodology is as follows: The aircraft design, as well as the flight path used in this paper, is described in Section 2.1. The fluid–structure interaction model, which couples the structural and aerodynamic model, is described in Section 2.2.

2.1. Aircraft Model and Flight Path

An AWE system consists of different components, namely, an aircraft, a ground station and a tether to connect the aircraft to the ground station. In this work, the reference AWES model of Eijkelhof et al. [17] was used. The design of this reference system aircraft is visualized in Figure 1. With a wing area of 150.3 m^2, the investigated AWE system is designed to reach a power output in the order of 5 MW. The reference model is an academic model and has never been constructed; therefore, no experimental data on the model are available.

In this work, a vertical and circular flight path is considered, with radius r = 265.5 m. Its center is located at height h = 403 m above the ground (Figure 2). Two coordinate systems are defined to enable the rigid-body motion of the aircraft: one fixed to the ground, the global coordinate system; and one that moves with the aircraft, the body-fixed coordinate system (denoted with subscript b). The presence of the tether and its effect on tilt and flight path are neglected, such that the aircraft operates under perfect crosswind conditions, similar to the blade of a wind turbine. The implementation of rigid-body motion is explained in [21]. In our simulations, the aircraft flew at a constant flight speed of 80 m/s, which made the period of revolution T_l = 20.85 s. The values of flight path radius, height and speed were based on the optimized flight path presented in [7].

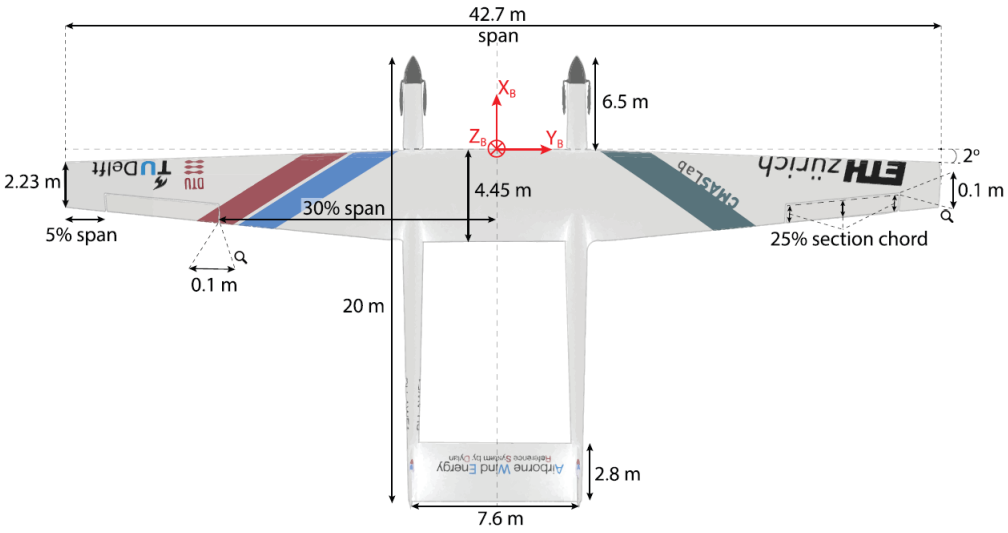

Figure 1. Multi-MW AWE reference system [16].

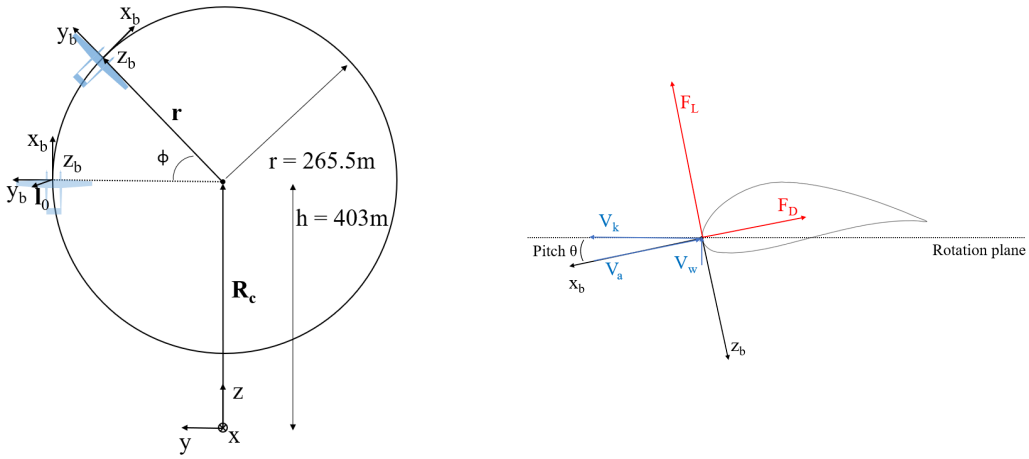

Figure 2. (**left**) Visualization of the prescribed flight path [21], chosen such that the aircraft operates under perfect crosswind conditions, similar to the blade of a wind turbine. (**right**) Visualization of aircraft attitude and forces.

2.2. Fluid–Structure Interaction Framework

In a fluid–structure interaction problem, the aerodynamic forces depend on the structural state. The structural state depends in turn on the aerodynamic loads, i.e., pressure and friction. For the FSI framework, a partitioned approach is used, meaning that separate models are used for fluid and structure, evaluated individually. A schematic of this partitioned approach is given in Figure 3. The contribution of frictional forces to the deformation of the structure is assumed to be negligible, such that the frictional forces are neglected. This partitioned FSI approach was performed with open-source Python code CoCoNuT, a coupling code for numerical tools developed at Ghent University [22]. The main building blocks of this approach are the aerodynamic and structural models, interpolation and the coupling algorithm. For the aerodynamic model and structural model, CFD and CSM software are used. The rigid-body motion of the crosswind flight maneuver in the aerodynamic model was achieved using a newly developed capability in CoCoNuT. This was performed by applying transformation matrices on the coordinates of the deformed wing using the Euler angle representation. To exchange data with the aerodynamic and structural model, solver wrappers are available in CoCoNuT. The output of the aerodynamic model, the loads, and of the structural model, the deformation is evaluated at the FSI interface, which is the

surface of the wing. Different meshes are constructed for the aerodynamic model and the structural model, hence interpolation at the mesh nodes is required to transfer data from one model to the other. Furthermore, a coupling algorithm is required to manage the data transfer. The details of interpolation and coupling are explained in Section 2.2.3.

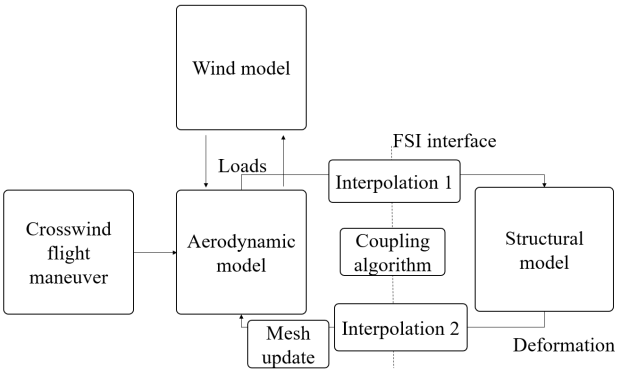

Figure 3. Overview of the partitioned FSI approach and interaction with sub-components to assess wing deformation of an AWE system in crosswind flight.

2.2.1. Structural Model

The Nastran® structural model is obtained from the reference model [7] and converted to an Abaqus® model. This is an FEM model of the composite wing consisting of skin, spars and ribs using 2D shell elements. The shell elements are composed of multiple composite skin panels. One panel consists of a [45°; −45°; 45°; 0°] ply orientation. The (−)45° ply has a thickness of 0.2 mm and Young's modulus of 3.83×10^{10} Pa in the longitudinal and lateral directions. The 0° ply has a thickness of 1.7 mm and Young's modulus of 1.12×10^{11} and 6.9×10^{9} Pa in the longitudinal and lateral directions, respectively. The density and Poisson's ratio of both materials are 1600 kg/m^3 and 0.3, respectively. The stringers, fuselage and tail were modeled using beam elements (see Figure 4). The mesh consists of 23,945 nodes and 55,780 elements, of which 3124 are linear Timoshenko beam elements, 250 are linear, quadrilateral shell elements and 52,406 are linear, triangular shell elements. A more detailed description of the complete structural model can be found in [7,17].

The aircraft is clamped in the middle at the spars (indicated in red) and is subjected to the aerodynamic loading (pressure) on the main wing. The pulling force of the tether on the airframe is neglected. For now, the rigid-body motion is not included in the structural model. Therefore, inertial and gravitational forces are neglected in the structural model. The effect of these forces on structural deformation is assumed to be small. The structural model calculates the deformation at each element, which is passed on to the aerodynamic model. As a result, the deformation at the left and right tips can be considered. The deflection at the tip is defined by averaging the deformation in the body z-direction of the nodes at the leading and trailing edge of the tips. The twist angle is calculated with the sine of the difference between the deformation of these nodes divided by the tip chord.

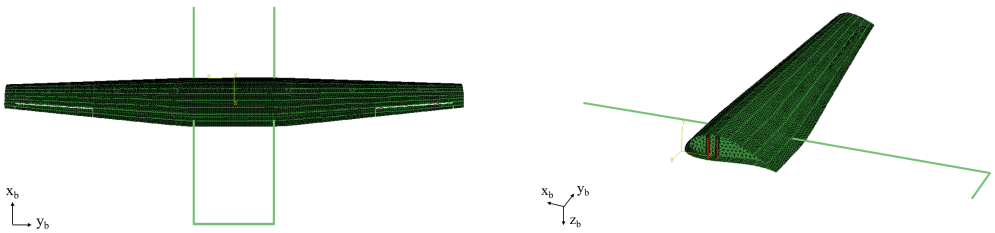

Figure 4. (**left**) Structural model and (**right**) cross-section view. The red lines indicate the clamping location.

2.2.2. Aerodynamic Model

The aerodynamic behavior of the wing of the reference aircraft is evaluated using CFD to predict the aerodynamic loads on the wing. The model is built such that both the flexible deformation and rigid-body motion of the wing can be taken into account. This is performed by decoupling the mesh near the wing (wing component mesh) from the mesh further away (background mesh) by means of the Chimera/overset technique. This technique then overlays the meshes and interpolates at the overset boundary. The deformation of the wing component mesh makes flexible motion of the wing possible. The tail and fuselage are not considered in the aerodynamic model, as the contribution of these elements to the aerodynamic loads is assumed to be negligible. A description of the solver and mesh settings is given in the remainder of this section.

Flow solver settings: The flow field is determined using incompressible unsteady Reynolds Averaged Navier–Stokes (URANS) simulations using the k-ω SST turbulence model and wall functions to model the boundary layer for both the wing and the ground. Pressure–velocity coupling is realized using a coupled scheme. The convective terms in the momentum equations are discretized in space using a first-order upwind scheme. Time integration is performed using a first-order implicit scheme with a time step of 0.02085 s. The following boundary conditions are imposed at the background domain: a velocity inlet, specifying the velocity; turbulent kinetic energy k; specific dissipation rate ω; a pressure outlet, where a 0 gauge pressure is imposed. The ground is defined as either a symmetry boundary or a no-slip wall with roughness height z_0 = 0.5 m, depending on the configuration. On the side and upper boundaries, a symmetry boundary condition is imposed.

Wind model: In this work, the neutral atmospheric boundary layer is modeled either as uniform inflow or as a logarithmic inlet profile in order to analyze the effects of changing wind conditions on height. In the latter case, the velocity profile as a function of height z is given by

$$u = \frac{u_*}{\kappa} \ln\left(\frac{z + z_0}{z_0}\right). \tag{1}$$

where u_* = 0.62554 m/s is the friction velocity, which represents the reference velocity scale of the wind; κ = 0.42 is the Von Karman constant; and z_0 = 0.5 m is the roughness height of the ground surface, representative of a landscape that features rather large obstacles separated by open space [23]. The combination of u_*, z_0 and κ results in a wind speed of u = 10 m/s at the average height of z = 403 m of the flight path.

A common challenge of simulating wind profiles in RANS simulations is the inconsistency between inlet profiles and the rough-wall formulation [24]. Efforts in the literature have been made to construct turbulence profiles for the k-ϵ model to mitigate this inconsistency, with ϵ being the turbulent dissipation rate. However, the k-ω SST turbulence model is used in this work. To the knowledge of the authors, efforts to construct turbulence profiles using the k-ω SST models are limited to [25]. Yang et al. [25] proposed the following inlet profiles for turbulent kinetic energy k and dissipation rate ω in order to satisfy the turbulence model equations:

$$k = \frac{{u_*}^2}{\sqrt{C_\mu}} \sqrt{C_1 \ln\left(\frac{z + z_0}{z_0}\right) + C_2} \text{ and } \omega = \frac{u_*}{\kappa \sqrt{C_\mu}} \frac{1}{z + z_0}. \tag{2}$$

where $C_1 = -0.04$ and C_2 = 0.54 are two constants that represent the inflow turbulence level and C_μ = 0.09 is a constant of the k-ϵ model [24].

As can be seen in Figure 5, there is still some inconsistency in the wind profile throughout the domain, particularly in the bottom part of the boundary layer, below 200 m for the profile at the outlet and below 100 m for the profile on the flight plane. However, as the aircraft does not fly below 137.5 m, the inconsistency between the profile at the inlet and on the plane where the aircraft flies is acceptable in the range of flight.

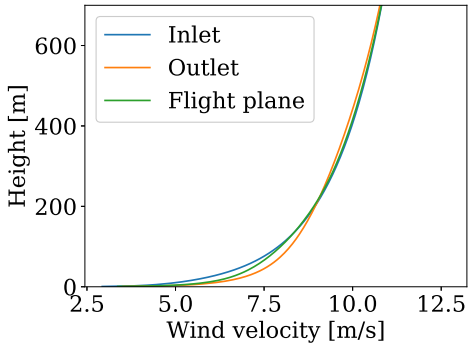

Figure 5. Resulting wind velocity profile at inlet, outlet and plane of flight.

Background mesh: A Cartesian background is created to simulate atmospheric wind conditions. As mentioned above, the atmospheric boundary layer is either modeled as a uniform or logarithmic inflow. The extent of the domain is chosen such that upstream flow induction and downstream wake development are unperturbed. Based on the rules of thumb for conventional wind turbine simulation [26], the size of this domain is extended by 5 times the path diameter both in front and above the system and 10 times the path diameter behind it. The mesh is visualized in Figure 6. Inside this large domain, mesh refinement is applied in a cuboid with dimensions $620 \times 620 \times 100$ m that is centered on the flight path. Within this cuboid, the mesh consists of cubical cells with an edge size of 4 m, which is 10% of the wing span. The total number of cells in the background mesh amounts to 6.9×10^6. The height of the first cell from the ground wall is around 1.5 m.

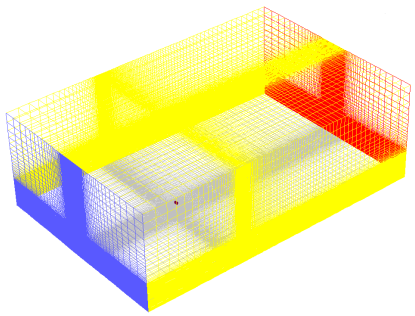

Figure 6. Background mesh (H = 2655 m, W = 5310 m, L = 7965 m). Blue, velocity inlet; red, pressure outlet; gray, no-slip wall; yellow; symmetry b.c.; purple, component mesh boundary with overset b.c.

Wing component mesh: A structured mesh with C-topology is developed to capture the flow close to the aircraft wing, as shown in Figure 7. A cross-section of the mesh domain consists of a semi-circle encompassing the wing and a rectangular domain capturing the near wake. The semi-circle is centered on the trailing edge of the wing root section and has a radius of 20 m. The dimensions of the rectangular box are 30×40 m. The 2D domain is subsequently extruded by 40 m along the lateral axis towards both tips.

In order to accurately simulate the boundary layer at the wing surface and capture flow separation, y^+ values in the order of 1 are required. However, this requires the mesh size at the wall to be very fine, which is very challenging in combination with mesh deformation methods, as the smallest grid cells can be squeezed. Instead, it is opted for using wall functions. The resulting mesh consists of 2.6×10^6 cells. A histogram of y^+ values at the wing surface is given in Figure 8, and the average y^+ value is 72. The mesh refinement in the interior of the component mesh is chosen such that changes in inflow quantities such as velocity and pressure are resolved. Finally, the mesh cells are not skewed and grow smoothly in size. The division of cells and growth rate are chosen such that the above requirements are met. From the wing surface to the overset boundary in front, in the upward and downward directions, the domain is divided into 38 cells, with a growth

rate of 1.248. From the wing surface to the overset boundary in the backward direction, the domain is divided into 59 cells, with a growth rate of 1.153. The upper and lower wing surface are divided into 60 cells in the chordwise direction, with a growth rate of 1.1, such that the leading and trailing edge are refined. In the spanwise direction, the wing surface is divided into 70 cells, and a bias factor of 4 is used to refine at the tips. This is visualized in Figure 8.

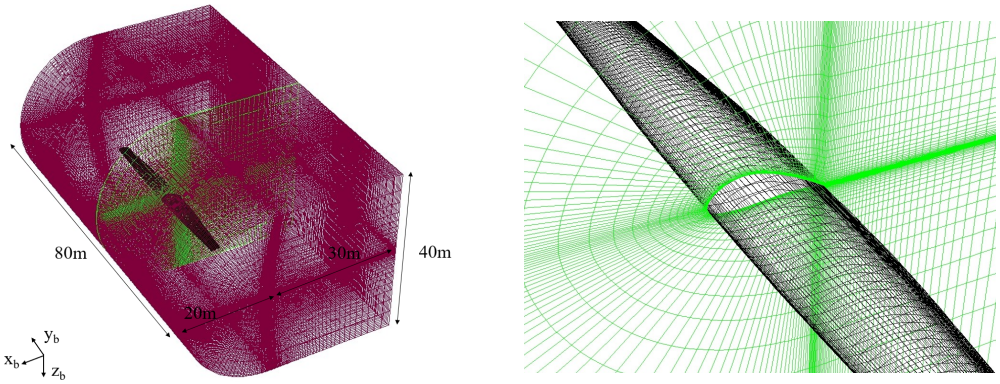

Figure 7. Wing component mesh. Purple, component mesh boundary with overset b.c.; green, internal intersection; black, wing surface with no-slip wall b.c.

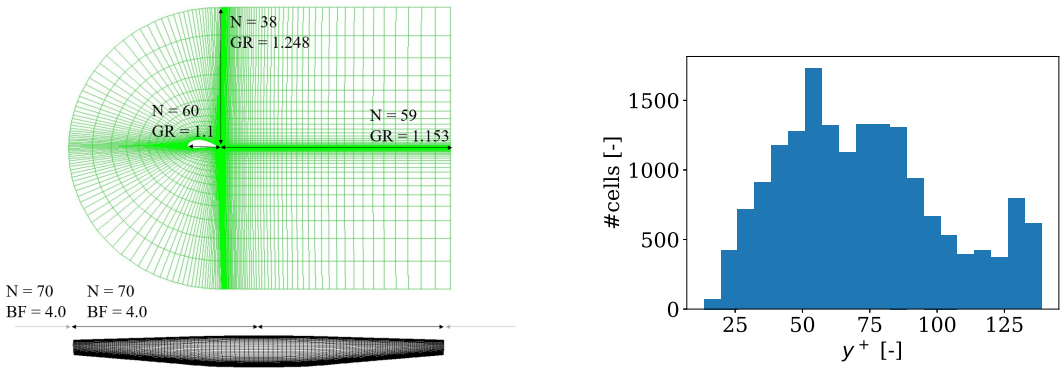

Figure 8. (**left**) Division of cells and growth rate (N = number of divisions, GR = growth rate, BF = bias factor). (**right**) Histogram of y^+ values (flight speed of 80 m/s, $\alpha = 0°$).

Chimera/overset technique: Separate meshes are developed to simulate the flow close to the wing (in the component mesh) and in the far-field wind flow (in the background mesh). The wing component mesh moves through the stationary background mesh according to the prescribed flight path. The Chimera/overset technique couples the two meshes at the intersection, the overset boundary, by interpolating the overlapping cells. This interpolation is updated while solving the flow equations. The meshes are constructed to have similar cell sizes (∼4 m) at the overset boundary to ensure good connectivity. The overset cell types are indicated in Figure 9. The cells in green are not used for interpolation and are directly solved by the RANS solver. The cells indicated in red are donor cells. The solution of these cells is passed to the blue cells, the receptor cells (of the other mesh). Both meshes have donor and receptor cells. In Figure 9, the large red cells are the donor cells of the background mesh, which pass information to the blue receptor cells of the component mesh at the overset boundary. The inner blue cells are the receptor cells of the background mesh. These cells receive information from the donor cells of the component mesh, which are hidden below the blue receptor cells of the background mesh.

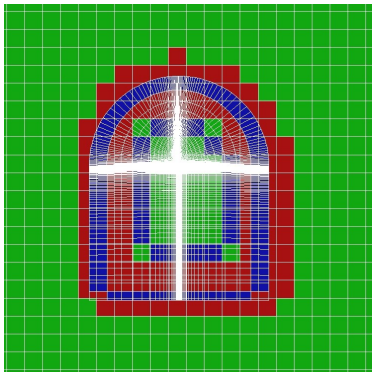

Figure 9. Chimera mesh connectivity. Green, solved cells; red, donor cells; blue, receptor cells. On the component mesh, only the receptor cells are indicated.

Mesh deformation: The wing component mesh should be able to move according to the flight path and also deform according to the structural deformations of the wing. To achieve the latter, the arbitrary Lagrangian–Eulerian (ALE) formulation is used, in which the mesh at the interface moves with the structure, while the interior of the component mesh moves arbitrarily, unrelated to structure or aerodynamics. A diffusion equation with a diffusion parameter of 1.5 is used to calculate the mesh deformation velocity. The diffusion is based on the normalized boundary distance from the wing surface. Boundary conditions for mesh displacement are obtained at the wing surface from the FSI model.

Aerodynamic model output: The output of the aerodynamic model is the pressure at each cell at the wing surface, which is passed on to the structural model. As a result, the pressure distribution is integrated along the chordwise direction to calculate the spanwise lift distributions. The total aerodynamic force coefficients are calculated, including friction. Flow quantities such as a normalized Q-criterion and velocity from the interior cells are used to visualize the wake flow.

Mesh independence study: The mesh independence study in this work on FSI is focused on local aerodynamics because this is the most critical aspect of this study. The structural mesh is given, so the mesh independence study is limited to steady aerodynamics. Four meshes are constructed for this study based on the finest possible mesh in the range of validity of wall functions. The finest mesh is indicated as ultra-fine in Table 2. A constant refinement factor of $\sqrt{3/2}$ is applied among all levels (ultra-fine, fine, medium and coarse) and is applied to the number of divisions. Mesh convergence can be observed in Figure 10. The lift coefficient changes only by 0.7%, and the drag coefficient changes by 4% in the last refinement, while the number of cells is almost doubled. The study shows that using a fine grid is a good compromise between accuracy and computational cost. Therefore, a fine grid is used in this work. The number of divisions of the fine grid is indicated in Figure 8.

Table 2. Description of meshes used for mesh independence study.

	Number of Cells
Coarse	0.76×10^6
Medium	1.40×10^6
Fine	2.56×10^6
Ultra-fine	4.76×10^6

2.2.3. Interpolation and Coupling Algorithm

For the fluid and structural models, different mesh topologies that are most suitable for each independently are used. These mesh cells do not match; therefore, interpolation at the interface is necessary. This is performed using bilinear interpolation in barycentric coordinates.

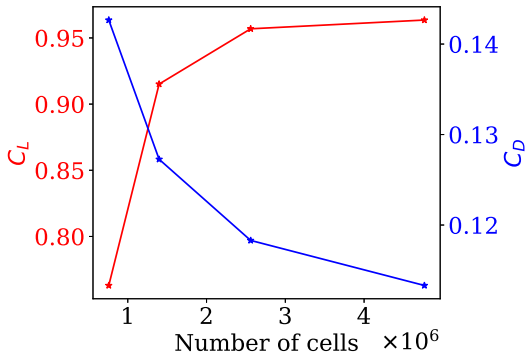

Figure 10. Lift and drag coefficient versus the number of cells in the component mesh.

Furthermore, an explicit approach is taken in this work to couple the different solvers, meaning that each solver is only evaluated once per time step. A schematic of the algorithm is given in Figure 11, where **x** represents the output of structural solver **S**, i.e., displacement at the interface; and **y** is the output of fluid solver **F**, i.e., aerodynamic loads at the interface. The output of the structural model at time step n, $\mathbf{x}^n$ is used to evaluate the aerodynamic loads at time step $n+1$, $\mathbf{y}^{n+1} = \mathbf{F}(\mathbf{x}^n)$. The output of the aerodynamic model of this time step is used to evaluate the structural displacement of the same time step, $\mathbf{x}^{n+1} = \mathbf{S}(\mathbf{y}^{n+1})$.

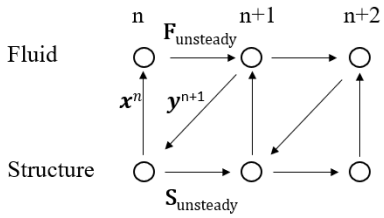

Figure 11. Schematic of the explicit coupling algorithm.

3. Results

In this section, the results are presented for three different configurations under different inflow conditions, as summarized in Table 3. In the first configuration, a uniform wind profile was applied at the inlet at a velocity of 10 m/s. In the second configuration, a logarithmic wind profile was applied at the inlet at a wind velocity of 10 m/s at the mean altitude of the flight path. In both configurations, the aircraft flew at speed $V_k = 80$ m/s and pitch angle $\theta = -7.125°$, which were chosen such that the angle of attack $\alpha = 0°$ when the incoming wind flow $V_w = 10$ m/s, assuming no induction (see Figure 2). The crosswind flight configurations were compared to a level-flight configuration with the same speed and angle of attack, referred to as configuration 0. In this configuration, the wing component mesh was used without background mesh, and the flight velocity was imposed at the inlet, which is the front of the wing component mesh. A more detailed analysis of configuration 0 and a comparison with other published results can be found in [21]. A lower lift coefficient was predicted by the presented CFD model compared with other published results [16] due to the inability of lower-fidelity models to predict flow separation.

Table 3. Flight configurations.

Configuration	Velocity Inlet (V_w)	Aircraft Speed (V_k)	Aircraft Pitch (θ)
0. Level flight	0 m/s	80 m/s	0°
1. Uniform wind	10 m/s	80 m/s	−7.125°
2. Logarithmic wind	Equation (1)	80 m/s	−7.125°

The total aerodynamic forces were calculated by integrating the resulting pressure and shear stress on the wing surface. The forces were normalized with the following reference values: The reference air density was ρ = 1.225 kg/m^3; the reference surface was planform area S = 150.3 m^2; and the reference speed was the local apparent speed assuming (V_a) no induction. A schematic of the lift and drag forces is given in Figure 2.

3.1. Unsteady Aerodynamics and Wake of a Starting AWE System

In this section, the results of unsteady aerodynamic simulations of a starting AWE system are presented. Here, the structural model is not coupled with the aerodynamic model, such that the results show rigid-wing aerodynamics and are further called CFD results.

During the CFD simulation, the AWE system wing performed a total of nine loops. In Figure 12, the lift and drag coefficients of the first and last loop are plotted for the different configurations. In configuration 1, the force coefficients did not change significantly with the loops. Compared with configuration 0, the lift coefficient was decreased by 2.3%, while the drag coefficient was the same. The decrease in lift can be explained by the existence of cross-flow as a result of circular motion. In configuration 2, the effect of the logarithmic profile on the aerodynamic performance is clearly visible in the plot. For the first half of the loop, the aircraft was in the upper half of the flight path where wind velocity is the highest, which increased the angle of attack and thus the lift coefficient. The opposite is true for the last half, when the aircraft flew at the bottom of the path.

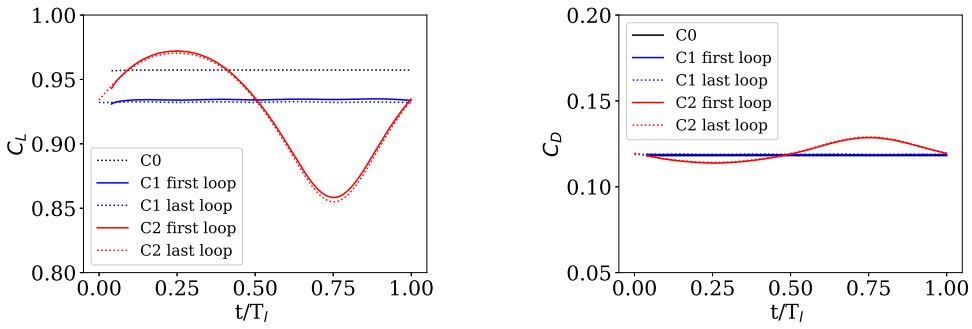

Figure 12. (**left**) Lift and (**right**) drag coefficients versus time for (C0) level flight, (C1) crosswind flight with uniform inflow and (C2) crosswind flight with logarithmic inflow.

In both configurations the following could be observed: The lift coefficient for the last loop was slightly lower than for the first loop, which could be explained by the induced flow. Most of this decrease in lift was observed in the first four loops; the flow field behaved steadily between loops 4 and 9 and was thus not expected to change after loop 9 (the last performed loop). The results of the last performed loop are referred to as the CFD results unless stated otherwise. The wake of the wing was transported downstream, as can be seen in Figures 13 and 14, and had no significant influence on the location of the aircraft (only 0.2%). The wake, visualized using the Q-criterion, disappeared, but the induced effect on the velocity remained. This could potentially reduce the efficiency of a system downstream.

The spanwise lift distributions are plotted in Figure 15 for different points in the last loop. The local lift coefficients were normalized with the local chord. The typical lift decrease at the tips was observed due to twist distribution and downwash. However, the distribution was skewed towards the wing section outside the circular flight path due to the larger velocity experienced here resulting from the rotating motion.

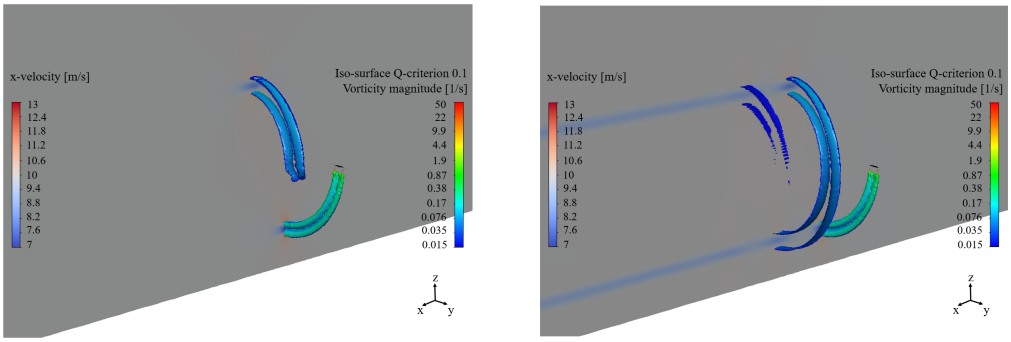

Figure 13. Visualization of the wake after (**left**) the first loop and (**right**) the last loop for the crosswind flight with uniform inflow. Note that the flow is from right to left. The contour plot shows the component of the wind velocity in the x-direction. The gray color indicates no disturbance; blue indicates velocity deficit; and red indicates velocity acceleration.

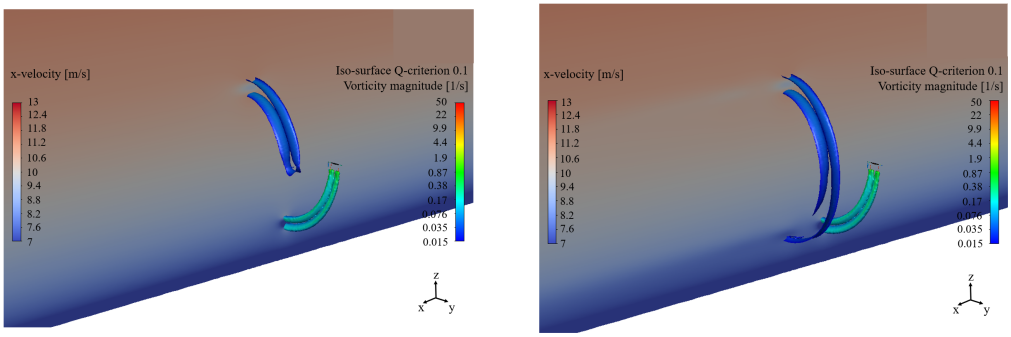

Figure 14. Visualization of the wake after (**left**) the first loop and (**right**) the last loop for the crosswind flight with logarithmic inflow. Note that the flow is from right to left. From the contour plot of the x-velocity, the logarithmic profile is clearly visible, but this is disturbed when the aircraft wing passes through this plane due to induced flow. From the flow field after the last loop, it can be seen that there is a velocity deficit in the downstream direction.

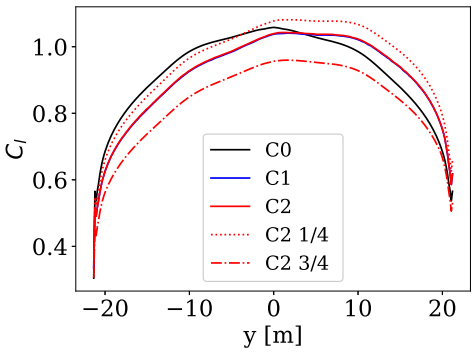

Figure 15. Spanwise lift distribution (last loop), with 1/4 meaning the highest altitude and 3/4 meaning the lowest altitude.

3.2. Crosswind Flight Simulations Including Fluid–Structure Interaction

In this section, the results of the simulations including fluid-structure interaction are discussed. These simulations were initialized with the results from the last loop in the CFD simulation (loop 9) discussed in the previous section. During the FSI simulations, the AWE system wing performed a total of two loops. No visible differences were observed between these two loops. The results are given for the last performed loop.

The aerodynamic force coefficients are plotted in Figure 16. The FSI results are compared with the CFD results. Overall, the FSI model predicted a slightly lower C_L than the CFD model (1.4%). This was due to the negative twist deformation of $-0.44°$ experienced

towards the tip inside the loop and −0.53° towards the tip outside loop. The offset with the CFD prediction remained constant due to the invariability of the twist deformation for both configurations. The spanwise lift distributions according to the FSI and CFD simulations are plotted in Figure 17 (right) for different points of the loop. Due to the negative twist, the local lift coefficient was reduced at the tips. This was more pronounced in the right wing, due to higher twist deformation, with right referring to the outside of the circular flight path. Due to the difference in twist deformation between left and right, the spanwise loading became more symmetric. This property could be used in future designs to make the spanwise loading more symmetric in a passive way, adding to the efficiency and safety of the aircraft.

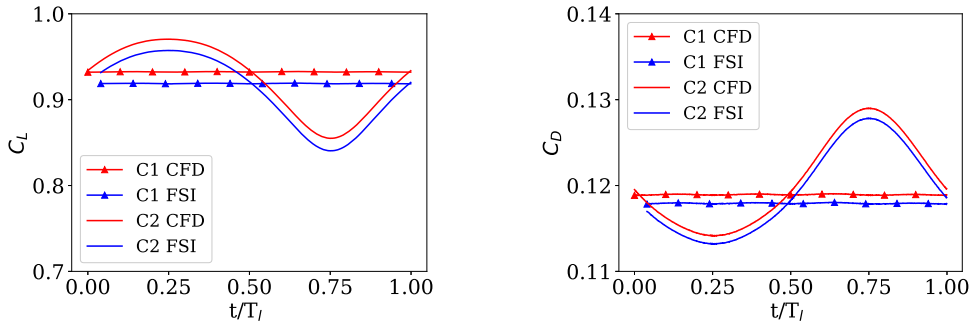

Figure 16. (**left**) Lift and (**right**) drag coefficients versus time for (C1) crosswind flight with uniform inflow and (C2) crosswind flight with logarithmic inflow. The FSI simulation predicted lower lift and drag coefficient in both configurations.

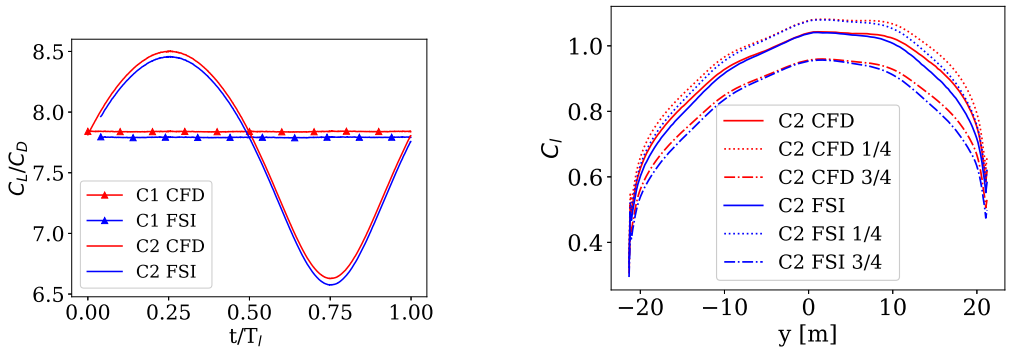

Figure 17. Lift over drag coefficients versus (**left**) time and (**right**) spanwise lift distribution, with 1/4 meaning the highest altitude and 3/4 meaning the lowest altitude.

The resulting deflection and twist deformation at the tip are plotted in Figure 18. Due to the asymmetric wing loading, there was a difference in deformation between the left and right wing tips of 16.4%. The right wing tip experienced more loading and thus deformation. Both tips were deflected with a negative twist. No aeroelastic instabilities were observed. The effect of the changing lift was visible in the deflection of the tip. However, twist deformation was barely affected by the change in lift. It could have been expected that the twist deformation would have decreased in the bottom part of the loop, together with deflection and lift. However, the decrease in the angle of attack also caused the center of pressure to move aft, which increased the twist deformation. This is visible in Figure 19 (right). Both effects canceled each other out; therefore, the twist deformation barely changed throughout the loop.

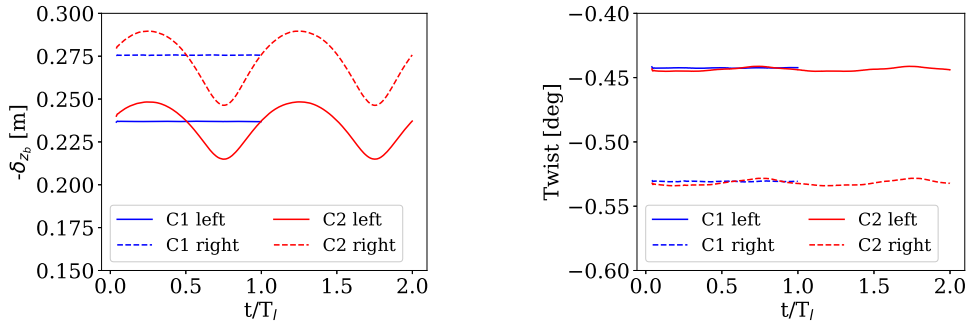

Figure 18. (**left**) Deflection and (**right**) twist deformation at the tip versus time for 1 loop (C1) crosswind flight with uniform inflow and 2 loops of (C2) crosswind flight with logarithmic inflow. The deflection for C2 varied with time; the twist deformation varied only slightly.

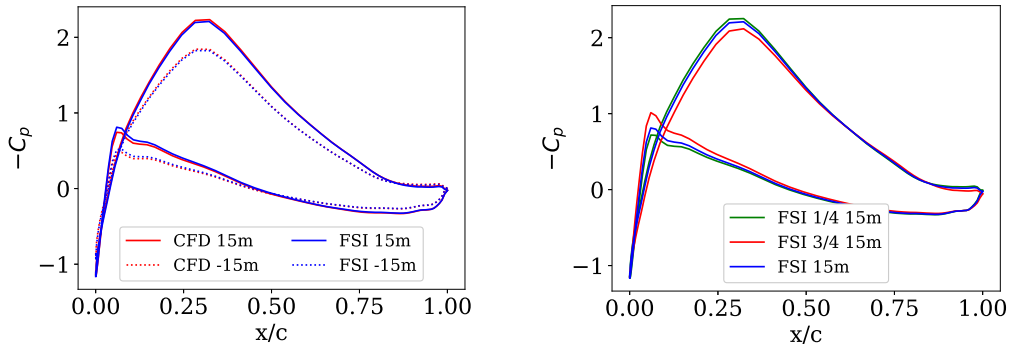

Figure 19. Chordwise pressure distributions for (C2) crosswind flight with logarithmic inflow at the chord 15 m and −15 m from the center of the wing.

The effects on the aerodynamic forces were limited, due to the high stiffness of the structure. However, for more flexible structures, the observed effects would likely be more pronounced.

3.3. Notes on Calculation Time

The unsteady aerodynamic simulations were performed using 392 cores on an AMD EPYC 7H12 64-Core system (VSC Tier-1 cluster). For the second configuration, the simulation took an average of 7.55 h to complete one loop. The unsteady FSI simulations under crosswind flight conditions were performed using 40 cores for the aerodynamic model and 12 cores for the structural model on a 2× 20-core Intel Xeon Gold 6242R 3.1 GHz system. For the second configuration, the FSI simulation took on average 75.6 h to complete one loop, from which 67.4% was taken by the aerodynamic model, 20.8% by the structural model and 11.8% by the coupling algorithm and overhead.

4. Conclusions and Outlook

A framework is presented to perform high-fidelity simulations of an AWE system. The framework applies the prescribed motion to the CFD model and couples it with the CSM model to perform high-fidelity FSI simulations in crosswind flight. The results showed that the crosswind motion of an AWE system in a CFD environment can be simulated in a robust way using the Chimera/overset technique.

The CFD results show a reduction in the lift coefficient due to crosswind motion of 2.3%. There was little effect of the induced flow on the lift coefficient (0.2%). The results show an asymmetric aerodynamic load distribution in crosswind flight with respect to level flight. Variations in lift and angle of attack were observed when performing crosswind flight in a logarithmic wind profile.

The FSI results show a reduction in the aerodynamic loads of 1.4% due to a negative twist deformation of $-0.44°$ at the left tip and $-0.53°$ at the right tip. There was a difference in twist deformation in the right and left wings of around 16.4% under the crosswind flight condition. Due to this difference, the spanwise loading became more symmetric. This property could be used in future designs to make the spanwise loading more symmetric in a passive way, adding to the efficiency and safety of the aircraft. Variation in the tip deflection was observed when performing crosswind flight in a logarithmic wind profile, due to the variation in lift. However, this variation was not observed in the twist deformation, due to the movement of the center of pressure. No aeroelastic instabilities were encountered in the simulations. The aeroelastic effects on the aerodynamic forces on the studied wing were limited, due to the high stiffness of the structure. However, for more flexible structures, the observed effects would likely be more pronounced.

Further work is directed towards the inclusion of rigid-body motion in the structural model and coupling the FSI model with a body dynamics model, in pursuit of physically feasible flight prediction and accurate simulation of power production.

Author Contributions: Methodology, N.P., T.H., J.W., G.C. and J.D.; Formal analysis, N.P.; Project administration, J.D.; Resources, J.D.; Supervision, T.H., J.W., G.C. and J.D.; Writing—original draft, N.P.; Writing—review and editing, T.H., J.W., G.C. and J.D.; funding acquisition, N.P., J.W., G.C. and J.D. All authors have read and agreed to the published version of the manuscript.

Funding: With the support of Energy Transition Fund of FPS Economy, project BORNE (Belgian Offshore aiRborne wind Energy).

Data Availability Statement: Not applicable.

Acknowledgments: The authors acknowledge Dylan Eijkelhof and Roland Schmehl for providing the necessary data of the reference model, more specifically the complete structural model and the data to replicate the aeroshell of the reference model. The computational resources in this work were provided by VSC (Flemish Supercomputer Center).

Conflicts of Interest: The authors declare no conflict of interest.

Abbreviations

The following abbreviations are used in this manuscript:

ALE	Arbitrary Lagrangian–Eulerian
AWE	Airborne wind energy
B.c.	Boundary condition
BF	Bias factor
CFD	Computational fluid dynamics
CSM	Computational structural mechanics
FSI	Fluid–structure interaction
GR	Growth rate
N	Number of divisions
RANS	Reynolds averaged Navier–Stokes
SST	Shear stress transport
URANS	Unsteady Reynolds averaged Navier–Stokes
VSC	Flemish Supercomputer Center
3DOF	Three degrees of freedom
6DOF	Six degrees of freedom

References

1. Diehl, M. Airborne wind energy: Basic concepts and physical foundations. In *Green Energy and Technology*; Springer: Berlin/Heidelberg, Germany, 2014; pp. 3–22. [CrossRef]
2. Echeverri, P.; Fricke, T.; Homsy, G.; Tucker, N. The Energy Kite: Selected Results from the Design, Development and Testing of Makani's Airborne wind Turbines. 2020. Available online: https://x.company/projects/makani/ (accessed on 1 November 2022).

3. Wijnja, J.; Schmehl, R.; Breuker, R.D.; Jensen, K.; Lind, D.V. Aeroelastic analysis of a large airborne wind turbine. *J. Guid. Control Dyn.* **2018**, *41*, 2374–2385. [CrossRef]
4. Haas, T.; Schutter, J.D.; Diehl, M.; Meyers, J. Large-eddy simulation of airborne wind energy farms. *Wind. Energy Sci.* **2022**, *7*, 1093–1135. [CrossRef]
5. Fasel, U.; Keidel, D.; Molinari, G.; Ermanni, P. *Aeroservoelastic Optimization of Morphing Airborne Wind Energy Wings*; AIAA SciTech Forum: San Diego, CA, USA, 2019. [CrossRef]
6. Candade, A.A.; Ranneberg, M.; Schmehl, R. Aero-structural design of composite wings for airborne wind energy applications. *J. Phys. Conf. Ser.* **2020**, *1618*, 032016. [CrossRef]
7. Eijkelhof, D. Design and Optimization Framework of a Multi-MW Airborne Wind Energy Reference System. Master's Thesis, Delft University of Technology, Technical University of Denmark, Delft, The Netherlands, 2019.
8. Castro-Fernández, I.; Borobia-Moreno, R.; Cavallaro, R.; Sánchez-Arriaga, G. Three-dimensional unsteady aerodynamic analysis of a rigid-framed delta kite applied to airborne wind energy. *Energies* **2021**, *14*, 8080. [CrossRef]
9. Folkersma, M.; Schmehl, R.; Viré, A. Steady-state aeroelasticity of ram-air wing for airborne wind energy applications. *J. Phys. Conf. Ser.* **2020**, *1618*, 32018. [CrossRef]
10. Viré, A.; Demkowicz, P.; Folkersma, M.; Roullier, A.; Schmehl, R. Reynolds-averaged Navier-Stokes simulations of the flow past a leading edge inflatable wing for airborne wind energy applications. *J. Phys. Conf. Ser.* **2020**, *1618*, 032007. [CrossRef]
11. Vimalakanthan, K.; Caboni, M.; Schepers, J.G.; Pechenik, E.; Williams, P. Aerodynamic analysis of Ampyx's airborne wind energy system. *J. Phys. Conf. Ser.* **2018**, *1037*, 062008. [CrossRef]
12. Kheiri, M.; Victor, S.; Rangriz, S.; Karakouzian, M.M.; Bourgault, F. Aerodynamic performance and wake flow of crosswind kite power systems. *Energies* **2022**, *15*, 2449. [CrossRef]
13. Hall, J. Aeroelastic Analysis of a Morphing Wing for Airborne Wind Energy Applications. Master's Thesis, Lund University, Lund, Sweden, 2017.
14. Kaufman-Martin, S.; Naclerrio, N.; May, P.; Luzzatto-Fegiz, P. An entrainment-based model for annular wakes, with applications to airborne wind energy. *Wind Energy* **2022**, 25, 419–431. [CrossRef]
15. Gaunaa, M.; Forsting, A.M.; Trevisi, F. An engineering model for the induction of crosswind kite power systems. *J. Phys. Conf. Ser.* **2020**, *1618*, 032010. [CrossRef]
16. Eijkelhof, D.; Rapp, S.; Fasel, U.; Gaunaa, M.; Schmehl, R. Reference design and simulation framework of a multi-megawatt airborne wind energy system. *J. Phys. Conf. Ser.* **2020**, *1618*, 032020. [CrossRef]
17. Eijkelhof, D.; Schmehl, R. Six-degrees-of-freedom simulation model for future multi-megawatt airborne wind energy systems. *Renew. Energy* **2022**, *196*, 137–150. [CrossRef]
18. Vermillion, C.; Cobb, M.; Fagiano, L.; Leuthold, R.; Diehl, M.; Smith, R.S.; Wood, T.A.; Rapp, S.; Schmehl, R.; Olinger, D.; et al. Electricity in the air: Insights from two decades of advanced control research and experimental flight testing of airborne wind energy systems. *Annu. Rev. Control* **2021**, *52*, 330–357. [CrossRef]
19. Santo, G.; Peeters, M.; Paepegem, W.V.; Degroote, J. Dynamic load and stress analysis of a large horizontal axis wind turbine using full scale fluid-structure interaction simulation. *Renew. Energy* **2019**, *140*, 212–226. [CrossRef]
20. Grinderslev, C.; Horcas, S.H.; Sørensen, N.N. Fluid—Structure interaction simulations of a wind turbine rotor in complex flows, validated through field experiments. *Wind Energy* **2021**, *24*, 1426–1442. [CrossRef]
21. Pynaert, N.; Wauters, J.; Crevecoeur, G.; Degroote, J. Unsteady aerodynamic simulations of a multi-megawatt airborne wind energy reference system using computational fluid dynamics. *J. Phys. Conf. Ser.* **2022**, *2265*, 042060. [CrossRef]
22. Degroote, J.; Annerel, S.; Vierendeels, J. Stability analysis of Gauss-Seidel iterations in a partitioned simulation of fluid-structure interaction. *Comput. Struct.* **2010**, *88*, 263–271. [CrossRef]
23. Wieringa, J. Updating the davenport roughness classification. *J. Wind. Eng. Ind. Aerodyn.* **1992**, *41*, 357–368. [CrossRef]
24. Parente, A.; Longo, R.; Ferrarotti, M. CFD boundary conditions, turbulence models and dispersion study for flows around obstacles. *VKI Lect. Ser.* **2017**. [CrossRef]
25. Yang, Y.; Gu, M.; Jin, X. New inflow boundary conditions for modeling the neutral equilibrium atmospheric boundary layer in SST k-ω model. *J. Wind. Eng. Ind. Aerodyn.* **2009**, *97*, 88–95. [CrossRef]
26. Sorensen, J.; Shen, W. Numerical modeling of wind turbine wakes. *J. Fluids Eng.* **2002**, *124*, 393–399. 1361. [CrossRef]